Mon. Not. R. Astron. Soc. **318**, 1206–1216 (2000)

High proper motion stars in Kapteyn Selected Area 94

J. A. Cooke[1★] and I. Neill Reid[2★]

[1]*Institute for Astronomy, University of Edinburgh, Blackford Hill, Edinburgh EH9 3HJ*
[2]*Department of Physics & Astronomy, University of Pennsylvania, 209 S. 33rd Street, Philadelphia, PA 19104-6396, USA*

Accepted 2000 June 26. Received 2000 June 9; in original form 2000 January 14

ABSTRACT

We have applied the astrometric techniques devised by Murray for analysis of 48-inch Schmidt photographic data to SuperCOSMOS scans of UK Schmidt plates centred on Kapteyn's Selected Area 94 ($\alpha = 2^{\rm h}\ 53^{\rm m}$, $\delta = 0°$). In this preliminary study, we combine astrometric data from four short-exposure *V*-band plates, taken in 1987 August (2 plates) and 1993 August (2 plates), with *BVRI* photometry from sky-limited plate material, to identify stars with proper motions exceeding 0.1 arcsec yr^{-1}. This paper discusses the completeness of the resulting sample and presents spectroscopy of 30 stars with $\mu > 0.2$ arcsec yr^{-1}. Based on the latter observations and the distribution in the [H_V, $(V - I)$] reduced proper-motion diagram, we have classified stars in the complete sample as candidate white dwarfs, main-sequence dwarfs and halo subdwarfs, and derived estimates of the disc and halo luminosity functions.

Key words: stars: low-mass, brown dwarfs – stars: luminosity function, mass function – astrometry/subdwarfs – Galaxy: structure.

1 INTRODUCTION

Two decades ago, Andrew Murray and co-workers (Murray & Corben 1979; Murray, Argyle & Corben 1986) presented results showing that Schmidt cameras could be used for accurate astrometric work, and gave examples of the potential of this technique for studies of the Galaxy (Murray 1986; Reid & Murray 1992). In terms of sheer accuracy, the *Hipparcos* astrometric satellite (Perryman et al. 1997) has surpassed photographic work, although for long time baselines the photographic archives still have considerable importance (e.g. Evans 1992; Evans & Irwin 1995) for proper-motion work, and the use of a large number of photographic measurements of the same field can improve the astrometric accuracy considerably over that from a single measurement of a single plate. Even relatively short exposure times, such as those used for the present work, enable the determination of astrometric parameters for stars 7 or 8 mag fainter than those at the completeness limits of the *Hipparcos* and *Tycho* catalogues, enabling complete samples of stars to be obtained to much greater distances than the *Hipparcos* sample, though at lower astrometric accuracy.

Undoubtedly, charge-coupled device (CCD) cameras will eventually replace the photographic emulsion completely; in terms of sensitivity they are a huge advance. However, as yet wide-field CCD images do not reach the coverage of a large Schmidt camera and here, again, the photographic data are still useful. We also posses large photographic archives and it is imperative that, at least for the present, we retain the ability to handle the data from these archives for comparison with future CCD measurements.

Combining measurements of many plates is in many ways similar to the plate stacking techniques used, for example, by Hawkins and co-workers (e.g. Knox, Hawkins & Hambly 1999). The latter methods, however, are aimed at detecting faint objects using differential astrometry, and do not provide the absolute kinematic measurements possible from a full astrometric analysis.

We present the first results obtained from a small part of a large dataset gathered over the period 1987–1994 for a project initiated by Andrew Murray aimed at the study of the kinematics of nearby stars. Over 250 plates were taken for this project, including around 70 astrometric plates in each of three fields, together with plates taken for photometric calibration.

2 ASTROMETRIC ANALYSIS

For this first sample of the data, we selected four plates in the field overlapping Kapteyn's Selected Area 94 (SA94), for which photometric calibration had already been obtained by one of us (INR). Two plates were selected at each end of the time sequence, with all four plates being taken at the same time of year. This meant that for this initial analysis the data could only be processed to obtain positions and proper motions, but not parallaxes; indeed, the effect of parallax was deliberately minimized by this selection of plate material, whilst maximizing the measured stellar motions. Details of the plates used are given in Table 1.

The plates were measured with the SuperCOSMOS machine, providing positions on the plate with a resolution of 0.01 μm, which is 10 times that available to Murray using the Galaxy

★ E-mail: j.cooke@roe.ac.uk (JAC); inr@morales.physics.upenn.edu (INR)

© 2000 RAS

Table 1. Photographic plates.

No.	Emulsion	Filter	Epoch	Exposure (m)
12069	IIaD	GG495	1987 Aug 15	20.0
12096	IIaD	GG495	1987 Aug 25	20.0
15701	IIaD	GG495	1993 Aug 14	20.0
15721	IIaD	GG495	1993 Aug 20	20.0

machine. Standard software was used to provide parameterized image data as part of the SuperCOSMOS measurement, together with the right ascension and declination for each object, currently derived using the ACT Reference Catalog (Urban, Corbin & Wycoff 1997). These positions make the pairing of objects on different plates a relatively easy task. Software was written to perform the pairing using an iterative technique, and is available as part of the SuperCOSMOS analysis software (Cooke 1997). The parameterized images on the four plates were paired and a master catalogue prepared by further pairing with the photometric standard stars, so that all stars used in the analysis had measures on all four astrometric plates, as well as photometric data.

The data reduction was undertaken using software originally written by Murray (Murray & Corben 1979) which uses the central overlap method (Eichhorn & Russell 1976). The solution we obtained was for position and proper motion only, since the plates had been selected purely for proper motions. A major improvement to the reduction process is that all the star data can now be analysed simultaneously, because computer performance is greatly improved over that available to Murray, who had to divide the stars into colour groups to limit the number of stars in any given solution, even with a total of 6125 stars. In our sample, the data for all 27 748 objects were handled in a single solution.

The output from this software is a catalogue of positions and proper motions, together with an analysis of statistical errors. For this analysis of four plates, the rms residuals in both right ascension and declination were around 0.10 arcsec, with a formal standard deviation in position for one unit weight measure of 0.14 arcsec. This gives an error in the calculated proper motions of ± 0.023 arcsec yr^{-1}.

Following the realease of the Tycho-2 Catalogue (Høg et al. 2000), the data were re-reduced to provide positions and proper motions on the *Hipparcos* system. This catalogue provided us with 557 positional standards over the field [compared with 133 from the PPM Catalogue (Röser & Bastian 1991) used for the first reduction]; we found excellent agreement between the results obtained from the two catalogues, with positions and proper motions as quoted in Table 2 virtually unchanged.

3 SAMPLE SELECTION

For this analysis we made no attempt to separate star and galaxy images. This has the advantages of simplicity and the certainty that all stars have been included, but the disadvantage of a significant contamination of the sample. We intend to perform star–galaxy separation in future runs and will check completeness at that stage.

We took the output catalogue produced as described above and sorted the objects contained in the catalogue into proper-motion order. To provide a careful check on the quality of the sample, the appropriate area was extracted from the Digitized Sky Survey (DSS, Daou et al. 1994), and for this field the digitized plates used were Palomar plates from 1955. Fields centred on each object

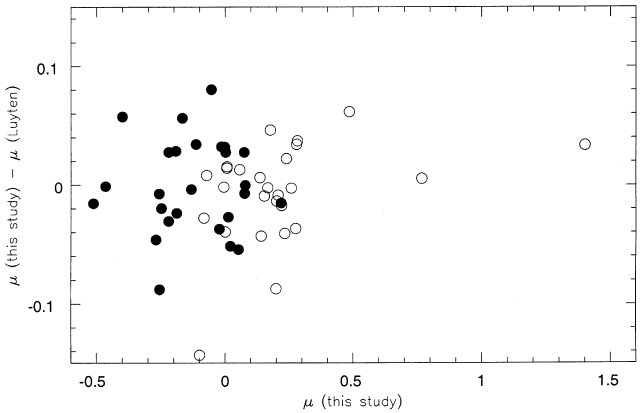

Figure 1. A comparison between our proper-motion measurements in RA (open circles) and Dec (filled circles), and Luyten's catalogued data for LHS and NLTT stars, in units of arcsec yr^{-1}.

were extracted from the DSS and printed for comparison with overlays of plots of the objects on the photometric plates at the two epochs. Because of the large time difference between the measured plates and those comprising the DSS data, proper motions for all of the stars amongst these objects were detectable by eye from the plots. Objects contaminating the initial sample were mainly obvious galaxies, where the short exposure times meant that the position centroids were badly affected by noise on the plates. A number of other objects that had been picked up as high proper motion turned out to be there because on one plate the measurement threshold for analysis of images had been set so that very close double images were often blended. This meant that two very close stars could appear as a single object on one plate, and be paired with one of the two stars on another plate, giving a false apparent proper motion. Most of these could be removed from the sample by using the residuals in position, but some remained. However, all objects down to a proper motion of 0.1 arcsec yr^{-1} were examined by eye to give a clean sample for follow-up work. This is presented as Table 2, which also contains the photometry except where we believe there may be problems. Most of the stars with problematic photometry are bright, suggesting a measurement or calibration problem, although of course some cases may be variable stars since the photometric plates were taken at different times. The astrometric results presented here are not affected significantly by photometric problems, since we are dealing only with objects having large proper motions. The $B - V$ colours are used, however, to take account of atmospheric refraction, so it is important that for later analyses the calibration is as accurate as possible.

For this clean sample, a comparison was made between the high proper-motion objects found and Luyten's NLTT Catalogue (Luyten 1979–1980). In general, good agreement was found between the proper motions obtained here and those given by Luyten; this comparison is shown in Fig. 1.

In the area of our measurements, there are 32 objects in the NLTT catalogue, three of which are also in Luyten's LHS Catalogue (Luyten 1979). All three of the LHS objects were detected, together with an additional 23 NLTT stars. The remaining six NLTT stars are identified in Table 3, together with details explaining their absence from our measurements. An additional 16 non-NLTT stars with proper motions large enough to appear in the NLTT were also found. Spectroscopy of a number of the latter objects is described in the following section.

4 SPECTROSCOPIC OBSERVATIONS

Low-resolution optical spectroscopy was obtained for 30 of the 37 stars with proper motions exceeding 0.2 arcsec yr^{-1}. The observations were made at Las Campanas Observatory between 1998 December 2 and 6, using the Modular Spectrograph mounted on the Du Pont 100-inch telescope. We employed a 600 line mm^{-1} grating, blazed at 7500 Å, and a Tektronix 1024 × 1024 format CCD as the detector. This configuration provides wavelength coverage from 6000 to 9500 Å at a dispersion of ∼1.9 Å pixel^{-1}. All of our observations were made with a 1.25 arcsec slit, giving a resolution of 3 pixels or 5.6 Å. We used a GG495 filter as an order-blocking filter to eliminate any contribution from second-order radiation.

All of the data were reduced using standard procedures in IRAF. The bias level was removed from each image using dark exposures, and the images flat-fielded using observations of the dome illuminated by incandescent lamps. The individual spectra were extracted using the *apextract* routine in IRAF. The wavelength calibration is determined from hollow cathode (Fe–Ar) and neon arc exposures taken at the start of each night: we did not intersperse calibration arcs throughout the observations since our goals did not include obtaing accurate radial velocities. A comparison of sky spectra shows that instrumental flexure seldom exceeds 1.5 pixels. Conditions were photometric throughout the observing run, with typical seeing of 1–1.3 arcsec, and we have used observations of the DC white dwarf L745-46A to set the data on a flux scale.

5 DISCUSSION

5.1 Spectral classification and the reduced proper-motion diagram

The sample of proper-motion stars selected in this survey is expected to consist primarily of lower main-sequence dwarfs from the disc and halo populations, together with a few white dwarfs. Our spectroscopic observations of the higher-motion stars confirm those expectations. We can quantify these results by using measurements of molecular bandstrengths to determine spectral types.

As originally established by Mould & Wyckoff (1978), decreasing metal abundance leads to reduced partial pressures and weakened bandstrengths for double-metal molecules, such as TiO, and reduced H^- opacity, because of the availability of fewer free electrons, but metal hydride molecular bands (MgH, CaH) retain their strength. Gizis (1997) has used this behaviour to define a quantitative classification system based on the relative strengths of the λλ6380, 6830 CaH bands and the full depth of the λ7050 γ(0,0) TiO band. Metal-poor stars are classified either as intermediate subdwarfs (sdK, sdM) or extreme subdwarfs (esdK, esdM), where the latter are of lower abundance (estimated as [M/H] < -1.5, Gizis & Reid 1998). We have measured the relevant indices, illustrated in Fig. 2a, for each of the SA94 proper-motion stars, and the results are given in Table 4. Fig. 3 compares those measurements against data for standard stars (from Gizis 1997), and the derived spectral types are given in Table 4. Three M dwarfs have Hα in emission, notably SA94-5617, which also exhibits He I λ6678 emission (EW = 1.5 Å, Fig. 2b). It is possible, even likely, that our observation of this star happened to catch it during a flare outburst. The equivalent widths for the Hα emission lines are listed in Table 4.

While we lack spectroscopic observations of the SA94 stars with $0.1 < \mu < 0.2$ arcsec yr^{-1}, we can use the available observations to calibrate the distribution in the reduced proper-motion diagram. Originally devised by Luyten, the Hertzsprung parameter

$$H_V = V + 5 + 5\log_{10}(\mu) = M_V + 5\log_{10}(V_T) - 3.38 \quad (1)$$

where V_T is the tangential velocity, provides a relation between the observed quantities of apparent magnitude and proper motion, and the intrinsic quantities, absolute magnitude and transverse velocity. Since the disc and the halo Galactic populations have distinct kinematic properties, there is a systematic (and substantial) offset in the respective mean velocities, $\langle V_T \rangle$, leading to an offset between the halo and disc sequences in the (H, colour) plane (Reid 1997).

Fig. 4 illustrates this classification technique using the [H_V, $(V-I)$] distribution of the SA94 proper-motion stars. Stars with known spectral types are identified and we plot reference sequences for the disc and halo. The latter have been computed under the assumption that the kinematics can be represented by a Schwarzschild velocity ellipsoid, that is, a Solar motion and Gaussian velocity dispersions. Table 5 lists the values adopted in these simulations: the halo kinematics are those derived by Layden et al. (1996) in their statistical parallax analysis of RR Lyrae motions; disc kinematics are cited for two analyses of volume-complete samples of M dwarfs within 20 pc of the Sun (Reid, Hawley & Gizis 1995; Hawley, Gizis & Reid 1996). Hawley et al. (1996) use maximum-likelihood techniques to derive a single-velocity ellipsoid; Reid et al. (1995) deconvolve the overall velocity distribution into two subpopulations using probability plots (Lutz & Upgren 1980), with ∼90 per cent of the local stars in the lower-velocity dispersion component. The latter approach represents better the high-velocity tail of the disc distribution, and is therefore more appropriate for the present analysis where kinematic selection effects are of considerable importance. It is tempting to label the latter two components as 'old disc' (low velocity) and 'thick disc' (high velocity), but there is no evidence for significant differences in chemical abundance: the local high-velocity outliers (heliocentric velocities exceeding 100 km s^{-1}) include Gl 53, Gl 213, Gl 447 and Gl 628, none of which is spectroscopically unusual.

Given an assumed velocity distribution, we can predict the expected median tangential velocities for SA94 ($l = 176°$, $b = -50°$). The fiducial [H_V, $(V-I)$] relations plotted in Fig. 4 are derived by offsetting the appropriate [M_V, $(V-I)$] relation for each kinematic subgroup by the value $\langle 5\log_{10}(V_T) \rangle$ listed in Table 5. Both disc components are represented by the mean colour–magnitude relation given by Reid & Gizis (1997), while the halo [M_V, $(V-I)$] relation is for the globular cluster NGC 6752 ([M/H] = −1.5, Thompson, private communication). As discussed in the following section, simulations based on these kinematics predict that few disc stars are expected to have velocities $V_T > 150$ km s^{-1}. The latter velocity corresponds to the dotted line plotted in Fig. 4, the disc colour–magnitude relation offset by $5\log V_T = 10.88$. That relation, combined with the distribution of spectroscopically classified stars, allows us to divide the full proper-motion catalogue into three subsets: probable main-sequence dwarfs, halo subdwarfs and white dwarfs.

5.2 Space densities and luminosity functions

The reduced proper-motion diagram allows an approximate

Table 2. SA94 proper-motion stars, $\mu > 0.1$ arcsec yr^{-1}.

SA94	J2000 RA	J2000 Dec	V	$B-V$	$V-I$	μ_α (arcsec yr^{-1})	μ_δ (arcsec yr^{-1})	μ_r (arcsec yr^{-1})	H_V	Comments	
23432	2:52:44.6	+1:55:56	14.67	1.60	1.94	1.400	−0.514	1.492	20.54	LHS	LHS 161
3616	2:50:06.5	−1:50:32	17.58	1.53	3.01	0.769	0.217	0.799	22.09	LHS	LHS 1451
627	2:46:30.6	−2:27:19	15.38	0.96	0.29	0.239	−0.466	0.524	18.98	LHS	LHS 1442
13427	2:48:43.2	+0:02:04	11.40		1.14	0.485	0.075	0.490	14.86	NLTT	
26466	3:01:05.8	+2:29:34	17.26	1.18	2.18	0.006	−0.402	0.402	20.27	NLTT	LP 591-231
5872	3:00:12.9	−1:25:03	15.25	1.09	1.83	0.302	0.011	0.302	17.65		
16223	2:43:00.4	+0:36:07	14.07	1.20	1.28	0.135	−0.270	0.302	16.47	NLTT	
21762	2:56:22.1	+1:37:50	18.27	1.37	1.88	0.154	−0.257	0.299	20.64	NLTT	LP 591-162
20999	2:43:21.8	+1:28:51	15.67	1.18	2.40	0.275	0.077	0.286	17.95	NLTT	LP 590-443
837	2:57:06.0	−2:25:08	9.97	0.97	0.83	0.282	0.012	0.282	12.22	NLTT	−3:466
25470	2:45:21.8	+2:18:12	14.73	1.15	2.63	0.279	−0.016	0.279	16.96	NLTT	
10093	2:56:03.7	−0:36:34	15.63	1.22	3.34	0.257	0.073	0.268	17.78	NLTT	LP 591-156
12173	2:52:15.8	−0:12:11	15.76	1.30	1.63	0.141	−0.220	0.261	17.85	NLTT	LP 591-94
8149	2:58:20.1	−0:59:31	10.67	1.85	1.80	0.007	−0.256	0.257	12.72	NLTT	
5617	2:55:09.3	−1:28:01	15.05	1.22	2.50	−0.006	−0.250	0.250	17.03	NLTT	
1618	2:50:45.1	−2:15:17	18.27	1.34	1.62	0.165	−0.176	0.241	20.18		
9635	2:41:14.0	−0:41:43				0.201	−0.134	0.241		NLTT	−1:377*
23011	2:44:58.7	+1:51:10	18.44	1.51	2.81	0.197	0.126	0.234	20.30		
23522	2:55:33.1	+1:56:55	18.68	1.40	2.70	0.232	−0.023	0.233	20.53	NLTT	591-145
6437	2:49:14.0	−1:19:02	18.28	1.68	1.76	−0.154	−0.174	0.232	20.10		
2757	2:54:40.3	−2:00:39	14.11	1.14	2.17	0.166	0.162	0.232	15.93		
13511	2:45:34.5	+0:02:59	14.87	1.69	2.47	0.023	−0.230	0.231	16.69		
14027	2:59:53.3	+0:09:18	17.35	1.18	2.48	0.227	0.036	0.230	19.16		
8414	2:46:19.3	−0:56:00	16.99	1.38	2.70	−0.123	−0.192	0.228	18.77		
3163	2:58:53.1	−1:55:50	16.14	1.29	2.42	0.221	0.052	0.227	17.91	NLTT	LP 591-209
22910	2:53:23.7	+1:49:54	14.54	1.58	1.06	0.219	−0.050	0.225	16.30		
17696	2:40:48.2	+0:52:56	12.65		1.89	0.000	−0.220	0.220	14.36	NLTT	LP 590-405
5415	2:52:02.0	−1:30:16	12.93	1.80	1.85	0.208	−0.067	0.218	14.63		
26620	2:48:13.9	+2:31:22	17.79	1.40	1.40	0.121	−0.182	0.218	19.48		
5798	2:47:37.0	−1:25:56	17.11	1.34	1.46	0.183	−0.115	0.216	18.78		
24233	3:01:46.8	+2:04:49	17.50	1.03	2.41	0.152	−0.148	0.213	19.14		
2488	2:41:41.1	−2:04:22	15.02	1.33	2.15	−0.082	−0.195	0.211	16.63	NLTT	LP 590-420
7365	2:46:15.1	−1:08:40	16.79	1.27	2.20	0.210	−0.015	0.210	18.40		
23498	2:52:24.2	+1:56:39	17.64	1.04	3.07	0.209	0.002	0.209	19.25		
15661	2:42:31.0	+0:29:08	15.82	1.26	1.05	0.207	−0.003	0.207	17.40	NLTT	LP 590-426
1689	2:43:29.9	−2:14:21	18.60	1.44	2.56	−0.145	−0.141	0.202	20.14		
16355	2:59:45.1	+0:37:30	9.18	0.59	1.00	−0.073	−0.189	0.202	10.71	NLTT	+0:492
21659	2:46:01.3	+1:36:19	17.07	1.29	3.56	0.200	0.001	0.200	18.56	NLTT	591-23
11720	3:00:28.5	−0:17:34	10.46			0.158	−0.113	0.194	11.88		
25255	2:46:29.7	+2:15:47	13.57	0.86	0.80	0.078	−0.176	0.193	15.00		
19334	2:48:46.0	+1:10:52	16.12	1.09	2.78	0.161	−0.102	0.190	17.52		
15143	2:42:07.4	+0:22:49	18.34	1.31	2.68	0.177	−0.054	0.185	19.66	NLTT	590-427
17890	2:51:04.2	+0:55:06	10.63			0.059	−0.175	0.185	11.96		
14423	2:53:04.7	+0:13:47	17.36	0.35	0.32	0.056	−0.169	0.178	18.60	NLTT	591-101
26970	2:41:36.4	+2:35:10	10.29			0.153	−0.088	0.176	11.53		
17191	2:42:43.8	+0:47:18	16.96	1.41	2.35	0.092	−0.150	0.176	18.19		
20175	2:46:07.8	+1:19:47	15.69	1.23	2.00	0.168	0.036	0.172	16.86		
421	2:56:22.7	−2:29:57	16.52	1.32	1.69	0.170	−0.020	0.171	17.67		
11132	2:42:30.5	−0:24:05	13.12	1.82	0.36	0.123	−0.118	0.170	14.28		
10385	2:57:28.5	−0:33:17	11.38	1.00	0.89	0.170	0.001	0.170	12.53		
14314	2:47:24.8	+0:12:39	18.54	1.48	1.67	0.109	−0.127	0.168	19.67		
6635	2:48:29.2	−1:16:56	9.14			0.166	0.020	0.167	10.26	NLTT	−1:395
17145	2:59:11.7	+0:46:47	16.68	1.09	3.32	0.158	−0.036	0.162	17.72		
5370	2:53:00.5	−1:30:50	11.28	1.46	1.26	−0.017	0.160	0.161	12.32		
9076	2:46:29.1	−0:47:59	17.34	1.28	2.49	0.136	−0.087	0.161	18.37		
18163	2:51:05.0	+0:58:06	15.90	0.78	1.11	0.007	−0.160	0.160	16.92		
15756	2:48:05.2	+0:30:12	15.80	1.15	2.19	0.068	−0.144	0.160	16.81		
27674	2:41:42.5	+2:43:24	13.15	1.58	1.12	0.102	−0.123	0.160	14.14		
4206	2:51:14.1	−1:43:57	18.44	1.33	2.21	−0.021	−0.158	0.159	19.45		
19838	2:59:13.1	+1:16:22	17.66	1.36	1.70	0.151	−0.048	0.158	18.67		
25974	2:52:35.7	+2:24:05	12.90	1.16	0.81	0.099	−0.122	0.157	13.87		
20420	2:45:11.0	+1:22:36	13.54			0.156	−0.015	0.156	14.51		
24760	2:58:11.7	+2:10:16	17.64	1.07	2.93	0.071	−0.138	0.155	18.60		
14838	2:54:16.4	+0:19:18	11.65	1.27	1.02	−0.057	−0.143	0.154	12.59		
5784	2:56:06.4	−1:26:02	14.04	1.02	1.49	0.153	−0.021	0.154	14.97		
7509	2:41:20.8	−1:07:08	16.95	1.40	2.51	−0.018	−0.151	0.152	17.86		
263	2:48:35.8	−2:31:38	12.81	1.40	1.00	−0.100	−0.114	0.152	13.71	NLTT	651-14
25782	2:49:32.6	+2:21:55	15.92	1.26	1.79	0.003	−0.151	0.151	16.80		
17000	2:49:56.2	+0:44:54	17.83	1.46	1.68	0.002	−0.149	0.149	18.69		
22834	2:47:22.7	+1:49:07	13.94	1.25	1.76	0.148	0.001	0.148	14.80		

Table 2 – *continued*

SA94	J2000 RA	J2000 Dec	V	$B-V$	$V-I$	μ_α (arcsec yr^{-1})	μ_δ (arcsec yr^{-1})	μ_r (arcsec yr^{-1})	H_V	Comments
10702	2:57:44.8	−0:29:29	13.79	1.04	1.36	−0.005	−0.148	0.148	14.64	
5044	2:58:15.0	−1:34:28	10.37			0.121	−0.085	0.148	11.21	
16054	2:57:39.4	+0:34:03	9.76			0.137	0.050	0.146	10.62	
13294	2:53:20.9	+0:00:27	17.42	1.27	1.30	0.098	−0.108	0.146	18.25	
18080	2:44:10.4	+0:57:22	15.44	1.37	2.33	−0.052	−0.136	0.146	16.26	
16359	2:51:39.5	+0:37:35	17.04	1.25	2.84	0.080	−0.123	0.146	17.85	
15043	2:47:26.2	+0:21:32	15.66	1.24	2.29	−0.145	−0.011	0.145	16.49	
17622	2:45:35.8	+0:52:02	17.79	1.36	2.37	0.011	−0.144	0.144	18.59	
11640	3:00:20.5	−0:18:39	8.26			0.135	−0.050	0.144	9.06	
21784	2:55:42.7	+1:38:08	14.02	0.76	1.99	0.051	−0.135	0.144	14.81	
5998	2:56:31.3	−1:23:53	16.82	1.27	1.96	0.142	−0.016	0.143	17.60	
23745	2:54:59.4	+1:59:11	13.76	1.34	2.07	−0.042	−0.136	0.142	14.52	
13027	2:59:08.1	−0:02:22	14.36	1.03	1.71	0.142	−0.004	0.142	15.10	
14863	2:52:34.2	+0:19:30	15.29	1.31	2.08	0.124	−0.068	0.141	16.04	
2111	2:57:04.5	−2:08:48	17.12	1.14	2.65	0.141	−0.011	0.141	17.86	
25728	2:55:40.8	+2:21:11	10.68			0.127	0.057	0.140	11.40	
8711	2:53:50.6	−0:52:01	10.71	1.32	0.15	0.140	0.000	0.140	11.42	
987	2:51:28.7	−2:23:23	10.49	1.15	0.99	0.121	−0.066	0.138	11.19	
7036	2:51:22.2	−1:12:12	13.74	1.16	1.75	0.137	−0.020	0.138	14.44	
26802	2:40:59.6	+2:33:25	17.85	1.57	1.62	−0.118	0.071	0.137	18.53	
18062	2:59:56.4	+0:57:14	16.34	0.64	1.29	0.108	−0.084	0.137	17.01	
13561	2:47:46.2	+0:03:32	16.54	0.00	−0.30	0.128	−0.047	0.137	17.21	
27300	2:41:16.8	+2:39:08	12.80	0.49	1.02	0.007	−0.136	0.136	13.49	
7940	2:59:09.5	−1:01:47	13.62	1.45	1.57	−0.026	−0.134	0.136	14.29	
14455	2:57:19.7	+0:14:15	15.86	1.20	2.24	0.121	−0.060	0.135	16.48	
21869	2:54:54.1	+1:38:55	14.23			0.132	0.025	0.134	14.87	
11880	2:45:19.6	−0:15:33	11.08			0.130	0.033	0.134	11.71	
24733	2:56:28.3	+2:09:58	11.15	1.62	1.49	0.099	0.090	0.134	11.77	
12657	2:47:47.3	−0:06:44	13.73	0.99	2.10	0.031	−0.130	0.133	14.38	
397	2:45:17.4	−2:30:11	17.65	1.31	2.46	0.106	0.078	0.132	18.27	
8329	2:54:07.1	−0:57:07	15.67	1.20	2.38	0.078	−0.107	0.132	16.26	
20168	2:48:39.0	+1:19:45	11.85	1.85	0.79	0.006	−0.131	0.132	12.42	
1287	2:41:07.2	−2:19:13	17.66	1.49	1.82	0.100	0.083	0.130	18.19	
25405	2:56:09.5	+2:17:30	18.54	1.49	1.67	−0.067	−0.110	0.129	19.11	
15736	2:44:49.1	+0:29:53	10.41			0.121	−0.043	0.129	10.98	
20479	2:58:51.4	+1:23:18	16.82	0.95	2.77	−0.047	−0.120	0.129	17.38	
5935	2:45:03.5	−1:24:30	13.63	1.43	1.29	0.093	0.089	0.129	14.18	
3993	2:50:54.9	−1:46:19	14.95	1.21	2.07	0.057	−0.115	0.129	15.49	
21947	2:49:57.1	+1:39:45	17.60	1.31	2.56	0.098	0.084	0.129	18.14	
9328	2:52:37.7	−0:45:16	15.11	1.18	2.07	0.112	0.065	0.129	15.65	
20452	2:55:20.0	+1:23:01	16.15	1.11	2.20	0.101	−0.078	0.127	16.66	
5341	2:48:59.5	−1:31:16	15.21	1.28	2.07	0.114	−0.055	0.126	15.72	
9005	2:45:11.9	−0:48:45	16.03	1.33	1.84	−0.073	−0.103	0.126	16.53	
132	2:48:51.5	−2:33:22	17.29	1.30	1.01	0.087	−0.089	0.124	17.77	
21588	2:58:04.7	+1:35:39	13.66	0.93	1.35	0.101	−0.072	0.124	14.13	
10871	2:57:27.8	−0:27:22	16.33	1.15	2.09	−0.034	−0.119	0.124	16.78	
23139	2:53:36.8	+1:52:40	8.17			0.122	0.021	0.123	8.61	
29	2:57:01.0	−2:34:31	17.40	0.97	2.96	−0.030	−0.119	0.123	17.84	
6344	3:00:45.9	−1:19:53	15.79	1.14	2.10	0.103	0.065	0.122	16.23	
1430	2:48:34.2	−2:17:26	16.25	1.29	2.39	−0.038	−0.116	0.122	16.67	
17214	3:00:26.6	+0:47:36	16.64	0.94	1.66	0.031	−0.117	0.121	17.06	
14316	2:52:31.7	+0:12:41	16.54	1.25	2.50	0.060	−0.105	0.121	16.96	
27496	2:55:02.7	+2:41:27	15.78	0.76	1.44	0.066	−0.102	0.121	16.19	
7354	2:59:04.2	−1:08:48	15.33	1.08	2.50	0.018	−0.120	0.121	15.74	
1936	2:49:24.2	−2:10:50	16.79	1.35	2.42	0.099	−0.070	0.121	17.18	
14892	2:49:55.7	+0:19:57	17.28	1.42	1.95	−0.072	−0.096	0.120	17.69	
6434	3:01:19.8	−1:19:03	10.81			0.064	−0.101	0.120	11.21	
1753	2:59:12.9	−2:13:30	13.47	1.43	1.66	0.117	0.027	0.120	13.85	
2332	2:49:56.1	−2:06:17	12.68	1.83	0.93	0.114	0.037	0.120	13.06	
3341	2:59:14.2	−1:53:44	16.35	1.09	1.55	0.010	−0.119	0.119	16.75	
27611	2:45:56.6	+2:42:39	16.42	1.29	3.19	0.093	−0.074	0.119	16.78	
19310	2:41:41.4	+1:10:37	15.81	1.48	2.02	0.116	−0.022	0.118	16.16	
16452	2:46:27.6	+0:38:41	15.47	1.24	2.00	0.101	−0.060	0.118	15.79	
25474	3:00:43.8	+2:18:13	12.61	0.12	0.21	0.047	−0.107	0.117	12.96	
13007	2:59:06.4	−0:02:40	16.87	1.20	2.20	0.027	−0.114	0.117	17.21	
18248	2:51:36.9	+0:59:04	14.23	1.00	1.52	0.084	−0.082	0.117	14.57	
4990	2:48:40.7	−1:35:09	17.84	1.36	2.12	−0.069	−0.094	0.117	18.17	
6945	2:50:02.7	−1:13:24	17.27	1.37	2.72	−0.081	−0.084	0.117	17.60	
5071	2:41:56.1	−1:34:11	16.21	1.39	0.97	0.062	−0.098	0.116	16.53	
10377	2:42:35.7	−0:33:26	12.01	1.77	1.22	0.110	0.035	0.116	12.33	

Table 2 – *continued*

SA94	J2000 RA	J2000 Dec	V	$B-V$	$V-I$	μ_α (arcsec yr^{-1})	μ_δ (arcsec yr^{-1})	μ_r (arcsec yr^{-1})	H_V	Comments
5541	2:47:50.8	−1:28:50	14.29	1.66	1.71	0.111	−0.032	0.116	14.60	
3888	2:48:09.5	−1:47:19	15.06	1.60	1.80	0.111	−0.031	0.115	15.37	
19900	2:59:52.8	+1:17:08	17.37	1.39	2.78	−0.066	0.094	0.115	17.67	
15818	2:58:38.4	+0:31:03	15.29	0.92	2.63	0.113	0.023	0.115	15.59	
26890	3:01:17.0	+2:34:21	13.31	0.09	1.64	0.112	−0.028	0.115	13.60	
17597	2:43:09.4	+0:51:45	17.52	1.42	2.84	0.048	−0.104	0.115	17.81	
6975	2:54:00.3	−1:13:04	14.37	0.92	0.70	0.110	−0.034	0.115	14.65	
18465	2:43:18.0	+1:01:27	17.39	1.45	2.50	0.087	−0.075	0.115	17.64	
26608	2:48:59.3	+2:31:10	18.21	1.19	1.42	0.113	−0.016	0.114	18.48	
3031	2:51:22.7	−1:57:21	11.43	0.69	0.78	0.109	−0.029	0.113	11.70	
18153	2:43:45.3	+0:58:00	16.60	1.05	1.28	0.100	−0.052	0.113	16.85	
23971	2:48:55.3	+2:01:54	11.78	1.81	0.82	0.063	−0.093	0.112	12.03	
11211	2:42:26.1	−0:23:14	14.65	0.71	0.47	0.038	−0.105	0.111	14.87	
208	2:55:57.3	−2:32:30	17.17	1.39	1.34	0.048	−0.100	0.111	17.39	
13579	2:45:47.6	+0:03:52	12.76			0.110	−0.013	0.111	12.96	
19747	2:42:51.6	+1:15:18	17.69	1.46	2.25	0.110	−0.003	0.110	17.89	
19274	2:53:09.0	+1:10:18	17.95	1.48	2.59	0.082	−0.073	0.110	18.14	
12745	2:58:22.4	−0:05:47	15.75	1.20	2.38	0.109	0.018	0.110	15.93	
17450	2:54:06.9	+0:50:11	15.98	1.22	2.33	0.063	0.088	0.109	16.19	
9893	2:41:35.0	−0:38:59	12.40	1.05	0.03	0.098	−0.049	0.109	12.59	
3083	2:56:23.9	−1:56:45	17.41	1.03	1.16	−0.022	−0.107	0.109	17.60	
5399	2:46:43.4	−1:30:32	17.78	1.23	2.66	−0.065	−0.088	0.109	17.97	
27032	2:44:28.8	+2:35:58	14.80	0.97	2.37	0.076	−0.078	0.109	14.99	
6259	2:50:08.9	−1:20:53	18.45	1.42	2.39	−0.033	−0.104	0.109	18.64	
12094	2:49:16.3	−0:13:12	18.34	1.45	2.38	0.025	−0.106	0.109	18.52	
4523	2:53:37.9	−1:40:32	9.64			0.107	−0.015	0.108	9.78	
24242	3:01:26.8	+2:04:50	14.07			0.063	−0.085	0.106	14.17	
5073	2:49:52.7	−1:34:08	16.27	1.43	2.91	0.031	0.101	0.105	16.40	
6517	2:47:54.9	−1:18:08	13.06	1.91	0.82	0.102	−0.023	0.105	13.18	
8435	2:41:50.0	−0:55:43	16.32	1.29	1.44	0.105	−0.002	0.105	16.43	
23006	2:50:39.2	+1:51:03	14.54	0.08	0.81	0.066	−0.081	0.105	14.65	
14306	2:53:37.8	+0:12:32	18.42	1.15	1.16	−0.047	−0.093	0.105	18.52	
5560	3:00:31.1	−1:28:37	17.11	0.98	2.71	−0.056	−0.088	0.104	17.20	
18796	2:47:14.9	+1:04:44	17.46	1.46	2.37	−0.097	−0.037	0.104	17.54	
6571	2:50:03.4	−1:17:36	13.59	1.00	1.09	0.028	−0.099	0.103	13.67	
11125	2:48:49.6	−0:24:13	18.04	1.42	2.12	−0.094	−0.043	0.103	18.11	
10095	2:54:26.5	−0:36:33	13.53	0.40	0.77	0.085	−0.058	0.103	13.59	
10156	3:01:39.0	−0:35:51	14.63	1.29	2.10	−0.103	−0.010	0.103	14.69	
735	2:45:13.5	−2:26:02	11.55	1.12	0.33	0.078	0.068	0.103	11.60	
8101	2:44:01.1	−1:00:05	12.23	1.49	0.87	0.102	0.013	0.103	12.27	
11847	2:42:33.1	−0:15:55	10.51			0.014	−0.102	0.103	10.54	
9079	2:53:56.1	−0:47:55	12.32	0.31	0.74	0.068	−0.075	0.102	12.37	
18526	2:50:52.7	+1:02:04	17.19	1.37	1.83	−0.062	−0.081	0.102	17.24	
21790	3:00:08.2	+1:38:11	14.80	1.26	2.85	0.097	0.032	0.102	14.84	
19495	2:57:26.4	+1:12:34	16.85	1.27	2.75	0.045	−0.091	0.102	16.87	
14460	2:59:53.3	+0:14:18	15.96	0.97	1.94	0.080	−0.061	0.101	16.02	
8393	2:43:23.7	−0:56:14	15.71	1.41	1.82	0.100	−0.018	0.101	15.73	
23887	2:55:25.2	+2:00:53	15.40	0.17	1.19	0.030	−0.097	0.101	15.42	
24323	2:55:33.9	+2:05:43	12.90			0.012	−0.100	0.100	12.90	

separation of disc and halo. We can combine our simulations of the expected kinematics with the available photometry to reconstruct the respective luminosity functions, estimating absolute magnitudes from the appropriate [M_V, $(V-I)$] relations. Space densities, and hence $\Phi(M_V)$, can be derived given an estimate of the relevant selection function. The latter can be predicted from the velocity distributions of disc and halo (for present purposes, we shall not differentiate between intermediate and extreme subdwarfs) as modified by the magnitude limit of the current survey ($V < 18.5$).

The distance distribution of a stellar sample selected by proper motion, $\mu > \mu_{\rm lim}$, represents the convolution of the velocity distribution [$V_{\rm T} > V_{\rm T}({\rm lim})$, $V_{\rm T}({\rm lim}) \propto r^{-1}$] and the stellar density distribution [$N(r) \propto r^2\,{\rm d}r$]. We have used Monte Carlo simulations to predict the relevant distributions for disc and halo stars towards SA94. Fig. 5a plots the tangential velocity distribution for all stars in both populations. Since the halo has both high-velocity dispersion and low rotation, $f_{\rm halo}(V_T)$ extends to substantially higher velocities, leading to a significant probability of subdwarfs at distances of over 600 pc meeting our proper-motion criterion. Fig. 5b shows the expected distance distribution of SA94 stars with $\mu > 0.1$ arcsec yr^{-1}. As emphasized elsewhere (Hanson 1979; Reid 1984; Reid 1998), selection by proper-motion biases a sample towards stars with high velocities relative to the Sun, and therefore amplifies the contribution from a high-velocity population, such as the halo. The amplification factor is given by

$$A_\mu = \left(\frac{\langle V_{\rm T}^1\rangle}{\langle V_{\rm T}^2\rangle}\right)^3 \qquad (2)$$

where $\langle V_{\rm T}^1\rangle$ is the average tangential velocity of the higher-velocity population. In the case of the two disc components listed

Table 3. NLTT stars not present in Table 2.

NLTT	(NLTT, 1950) RA	Dec	Comments
+0:444	2:38:07	+0:58.9	PPM145804 – bright ($m_{pg} = 11.0$), not present in our photometric data
591-18	2:49:13	+0:42.8	Faint ($m_{pg} = 21.0$), not present in data for one astrometric plate
591-212	2:56:36	+1:35.8	Double? star close to NLTT position, but no large proper-motion object nearby
590-431	2:39:42	−2:33.5	PPM184933 – bright double star, images merged in astrometric data
−2:476	2:39:46	−2:33.9	PPM184933 – as above
	2:58:00	−1:37.0	Closest star to NLTT position has about the correct magnitude, but a much smaller proper motion

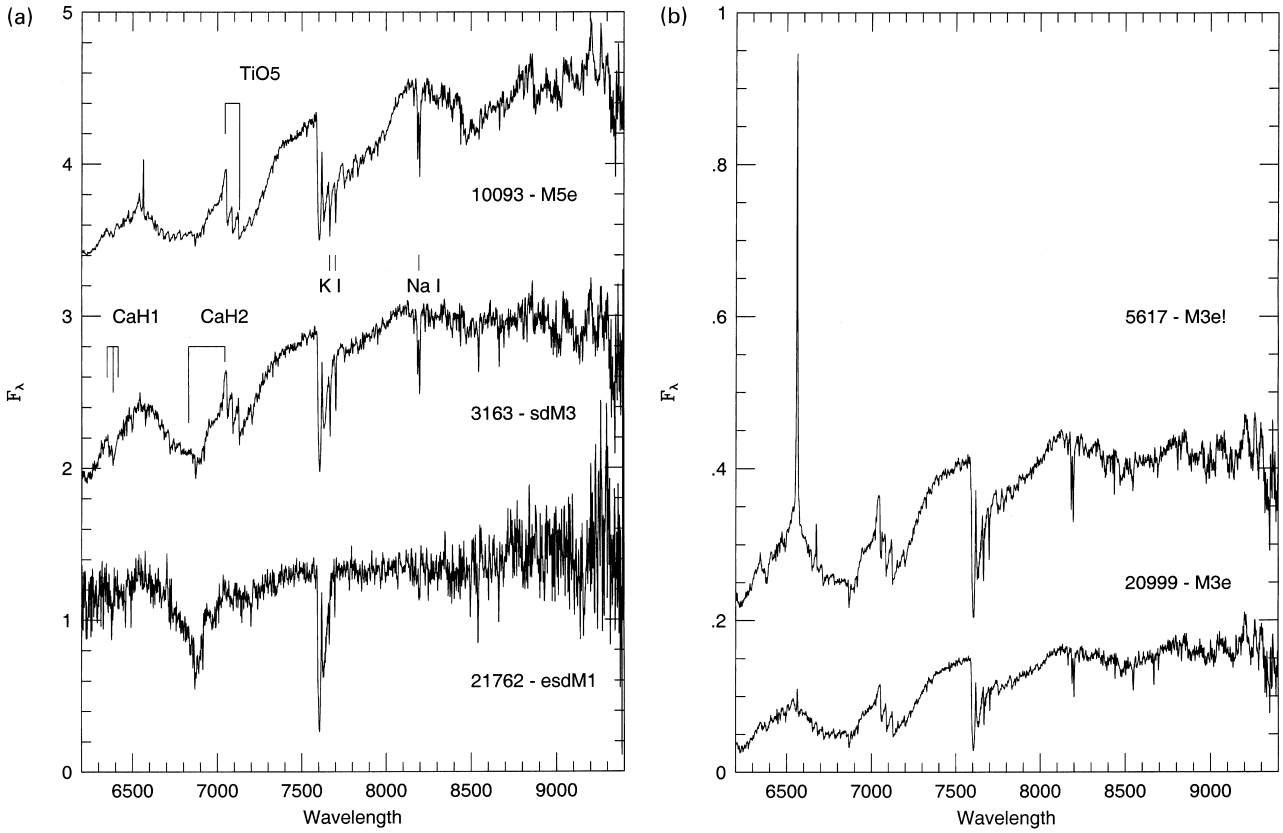

Figure 2. (a) Spectra of representative stars. The passbands for the TiO5 and CaH indices are indicated. (b) Spectra of the dMe dwarfs SA94-20999 and SA94-5617.

in Table 5, the contribution from the higher-velocity component is amplified by a factor of ∼5 in SA94, while for the halo, $A_\mu \sim 215$. The distributions plotted in Fig. 5b take that scaling into account: if the relative number densities of disc$_1$:disc$_2$:halo are 90:10:0.25 within a volume-limited sample, we expect number ratios of 2:1:0.65 (or $N_{halo}/N_{disc} \sim 0.2$) for a proper-motion limited sample.

Based on the simulations, 80 per cent of the stars in a proper-motion limited sample are expected to lie at distances of less than d_C (Reid 1998), where

$$d_C = \frac{\langle V_T \rangle}{\kappa \mu_{lim}} \tag{3}$$

and $\kappa = 4.74$. Given this result, we can determine whether stars of a given absolute magnitude can be regarded as a proper-motion limited sample or a magnitude-limited sample: i.e. is the distance limit set by the velocity distribution, or by apparent magnitude limit of the survey. Given the kinematics adopted here, $d_C \sim 111$ and ∼197 pc for the two disc components, and ∼670 pc for the halo (Fig. 5c), or distance moduli of 5.2, 6.5 and 8.4 respectively. Our sample has an effective magnitude limit of $V < 18.5$. Thus, disc dwarfs with $M_V > 12$ and halo subdwarfs with $M_V > 10$ constitute magnitude-limited samples; intrinsically more luminous stars constitute proper-motion limited samples.

Since $\mu \propto r^{-1}$, a decreasing fraction of any stellar component meets a given proper-motion criterion as one moves to larger distances. Fig. 5d shows the expected results for the disc and halo in SA94, where we plot the relative completeness, f_μ, of the proper-motion selected sample in a cumulative sense, i.e. the fraction of stars with $r < r_{lim}$ expected to have $\mu > 0.1$ arcsec yr^{-1}. Those distributions predict that 20 per cent of disc stars and 35 per cent of halo subdwarfs with distances less than the respective d_C should be detected. Thus, for proper-motion limited samples, we can estimate the space densities as

$$\rho_* = \frac{3}{\Omega} \frac{N_{tot} \times 0.8}{f_\mu \times d_C^3} \tag{4}$$

where Ω is the solid angle covered by the observations and

Table 4. Spectroscopic indices for SA94 proper-motion stars.

SA94	V	$V-I$	TiO5	CaH1	CaH2	CaH3	Hα (Å)	Sp
10093	15.63	3.34	0.307	0.786	0.319	0.600	4.2	M5e
12173	15.76	1.63	1.054	0.862	0.829	0.934		esdK7
13427	11.40	1.14	0.783	0.853	0.599	0.808		sdM1
14027	17.35	2.48	0.517	0.773	0.407	0.673		M3
15661	15.82	1.05	1.029	0.973	0.925	0.965		sdK5
1618	18.27	1.62	0.990	0.766	0.797	0.927		esdK7
16223	14.07	1.28	0.810	0.896	0.730	0.872		M0
1689	18.60	2.56	0.419	0.841	0.400	0.650		M4
17696	12.65	1.89	0.804	0.770	0.513	0.732		sdM2
20999	15.67	2.40	0.464	0.844	0.430	0.705	1.8	M3e
21762	18.27	1.88	0.986	0.906	0.676	0.796		esdM1
22910	14.54	1.06	1.067	1.001	0.881	0.943		DA
23011	18.44	2.81	0.491	0.837	0.437	0.728		M3
23432	14.67	1.94	0.926	0.745	0.608	0.788		esdM1, LHS 161
23498	17.64	3.07	0.500	0.874	0.410	0.699		M3
24233	17.50	2.41	0.580	0.788	0.512	0.768		M2
2488	15.02	2.15	0.589	0.857	0.463	0.744		M2
25470	14.73	2.63	0.514	0.762	0.453	0.702		M3
26466	17.26	2.18	0.876	0.921	0.721	0.904		sdM0
26620	17.79	1.40	0.977	0.912	0.744	0.871		sdM0
2757	14.11	2.17	0.593	0.886	0.445	0.721		M3
3163	16.14	2.42	0.637	0.746	0.436	0.659		sdM3
3616	17.58	3.01	0.297	0.687	0.369	0.599		M5, LHS 1451
5415	12.13	1.85	0.696	0.899	0.635	0.812		M1
5617	15.05	2.50	0.488	0.785	0.440	0.662	25.3	M3e!
5798	17.11	1.46	1.023	0.894	0.748	0.877		esdM0
627	15.38	0.29	1.070	1.004	0.830	0.940		DA, LHS 1442
6437	18.28	1.76	0.946	0.743	0.577	0.745		esdM1
7365	16.79	2.20	0.609	0.844	0.457	0.722		M2
8414	16.99	2.70	0.399	0.833	0.397	0.697		M4

$f_\mu = 0.27$ for the thin disc, 0.21 for the high-velocity disc and 0.40 for the halo. In the case of magnitude-limited, lower-luminosity stars, the distance limit is reduced and f_μ increased.

In many respects, this analysis can be considered the poor-man's version of Schmidt's (1975) $V/V_{\rm max}$ analysis. In the latter case, distances to the individual stars are known, allowing explicit calculation of both the enclosed volume and the limiting volume for each star; under the present circumstance, we can only group stars based on their photometric properties, and estimate the average density. The latter calculation is sensitive to the kinematics adopted, since the distance limit, $d_{\rm C}$, is directly proportional to the average tangential velocity, $\langle V_{\rm T}\rangle$, and the sampling volume varies as $(\langle V_{\rm T}\rangle)^3$.

We have used position in the reduced proper-motion diagram to segregate our sample into candidate halo and disc dwarfs (the dotted line plotted in Fig. 4). Individual stars are assigned absolute magnitudes based on the colour–magnitude relations used to derive the $[H_V, (V-I)]$ relations plotted in Fig. 4. Table 6 lists the number of stars classified as disc and halo in the present SA94 sample, and the appropriate values of $d_{\rm C}$ and f_μ, given the population kinematics listed in Table 5. We have used these data to derive $\Phi(M_V)$ for both disc and halo, allowing for the presence of two disc populations with distinct kinematics. We assume a local thin disc:thick disc number ratio of 9:1. Hence, at absolute magnitudes where both populations are proper-motion limited, two out of three stars classified as disc dwarfs are members of the lower-velocity thin disc; the ratio is scaled to the appropriate value in the magnitude-limited regime.

Fig. 6 shows the results of these calculations, where we match the luminosity functions deduced for the thin disc and halo against reference data from Reid & Hawley (2000: ch. 7, fig. 25 for the disc; ch. 11, fig 10 for the halo): the thick-disc function is, by definition, scaled to 11 per cent of the thin-disc values. The densities that we derive for the halo component at $M_V < 11$ are in good agreement with the reference data, which correspond approximately to a local halo-to-disc number ratio of 1:200. Our results at fainter magnitudes are higher than the reference values by an order of magnitude, probably due to our including misclassified disc dwarfs, or even cool white dwarfs, in the halo sample. Spectroscopy would permit more accurate classification.

In contrast, the densities derived for the disc component are a factor of 2 higher than the reference values, which are based on nearby-star data. The discrepancy likely rests with the kinematic model we adopt for the disc: an underestimate in either the mean velocity or in the proportion of higher-velocity stars in the wings of the distribution (i.e. a non-Gaussian distribution), leads to an underestimate in $d_{\rm C}$ and an overestimate in f_μ. As noted above, the sampling volume varies with $(\langle V_{\rm T}\rangle)^3$; f_μ, in contrast, decreases relatively slowly with increasing $d_{\rm C}$. Hence, increasing $\langle V_{\rm T}\rangle$ by 25 per cent would give good agreement between our analysis and the nearby star data. The low-velocity thin-disc population is most susceptible to this type of uncertainty: an error of $5\,{\rm km\,s^{-1}}$ in $\langle V_{\rm T}\rangle$ is more significant at $\langle V_{\rm T}\rangle = 50\,{\rm km\,s^{-1}}$ (disc) than $\langle V_{\rm T}\rangle = 180\,{\rm km\,s^{-1}}$ (halo).

Clearly, there are significant uncertainties associated with this analysis, as illustrated by the lower panel in Fig. 6. However, results for the higher-velocity halo population are more robust. Given a reliable determination of the velocity distribution of a stellar population, combined with spectroscopic observations of the complete sample, this method offers an alternative, if less direct, means of probing the stellar luminosity function, without requiring trigonometric parallax measurements for each star.

6 CONCLUSIONS

We have used the techniques devised by Murray et al. (1986) to undertake an astrometric analysis of SuperCOSMOS scans of four *V*-band UK Schmidt plates. The current study is limited to proper-motion measurements. With data spanning a baseline of 6 yr, we have derived motions accurate to ± 0.023 arcsec yr^{-1} and identified 189 stars with $\mu > 0.1$ arcsec yr^{-1}. The distribution of those stars in the [H_V, $(V-I)$] reduced proper-motion diagram suggests that a significant fraction are halo subdwarfs, a hypothesis supported by spectroscopic observations of 30 of the 37 stars with $\mu > 0.2$ arcsec yr^{-1}. The latter sample includes six very metal-poor subdwarfs and one extremely active M3 dwarf, perhaps caught in outburst. Adopting kinematic models for the disc and halo populations, we have used statistical techniques to derive estimates of the luminosity functions of both stellar populations.

We next propose to measure the remaining plates available for SA94 and perform a full astrometric analysis. Measurements are well underway and the next reduction phase will allow the determination of parallaxes as well as improved proper motions for the present sample of stars. We will also extend the analysis to two other fields with similar datasets, including UKST field 87, adjacent to the Large Magellanic Cloud. Combined, these scans will provide a substantial data set for study of the galaxy's dynamics, as well as for the identification of new interesting candidate nearby disc dwarfs, white dwarfs and halo subdwarfs.

ACKNOWLEDGMENTS

The authors are grateful to the staff of the Wide Field Astronomy

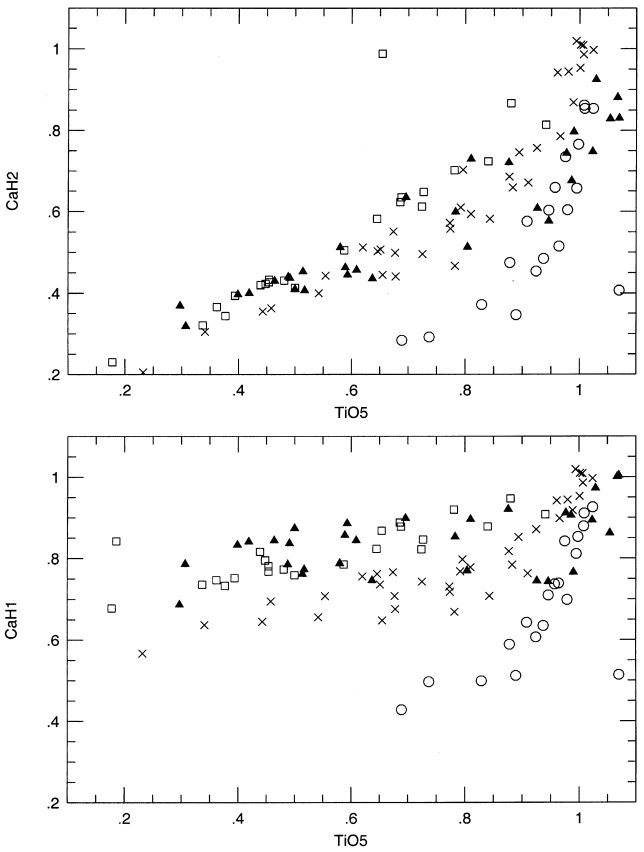

Figure 3. Molecular band indices for the SA94 stars matched against standards from Gizis (1997). Known disc dwarfs are plotted as open squares, intermediate subdwarfs as crosses and extreme subdwarfs as open circles. The SA94 stars are plotted as solid triangles.

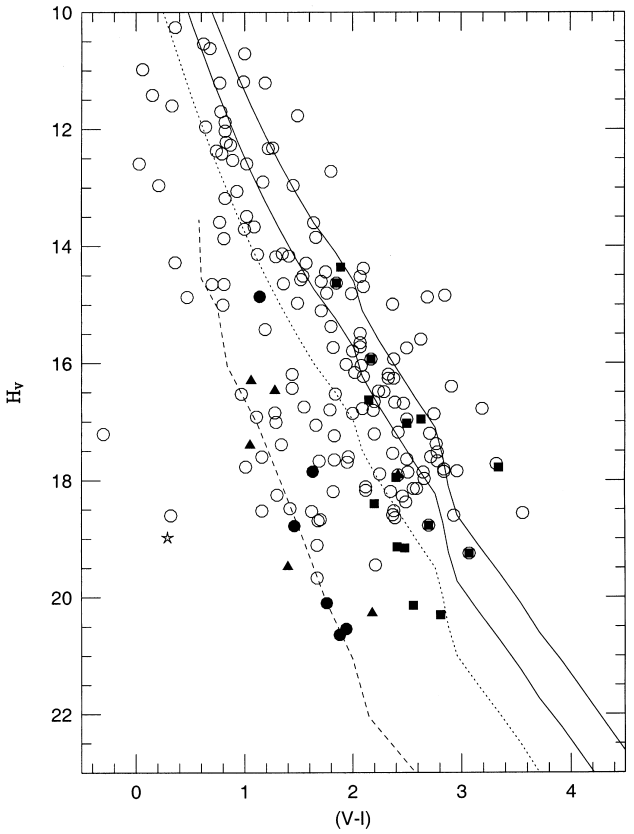

Figure 4. The reduced proper-motion diagram for the SA94 stars with $\mu > 0.1$ arcsec yr^{-1}. Solid squares are spectroscopically confirmed disc dwarfs; solid triangles, intermediate subdwarfs; solid points, extreme subdwarfs; and five-point stars, white dwarfs. The fiducial sequences are for the two disc components (solid line) and halo (dashed line) at the median tangential velocities given in Table 5, while the dotted line separates probable disc dwarfs and halo subdwarfs; the few white dwarfs in the sample form an obvious separate sequence.

Table 5. Stellar kinematics.

Population	$U_\odot$	$V_\odot$	$W_\odot$	σ_U	σ_V	σ_W	$\langle V_T \rangle$	$\langle 5 \log V_T \rangle$	Ref.
Halo	9	−210	−12	168	102	97	318	12.42	Layden et al. (1996)
Disc									
1-component	−10	−5	−7	41	27	21	52	8.41	Hawley et al. (1996)
2-component	−10	−23	−7	35	21	20	52.6	8.48	Reid et al. (1995)
				52	45	32	89.0	9.61	

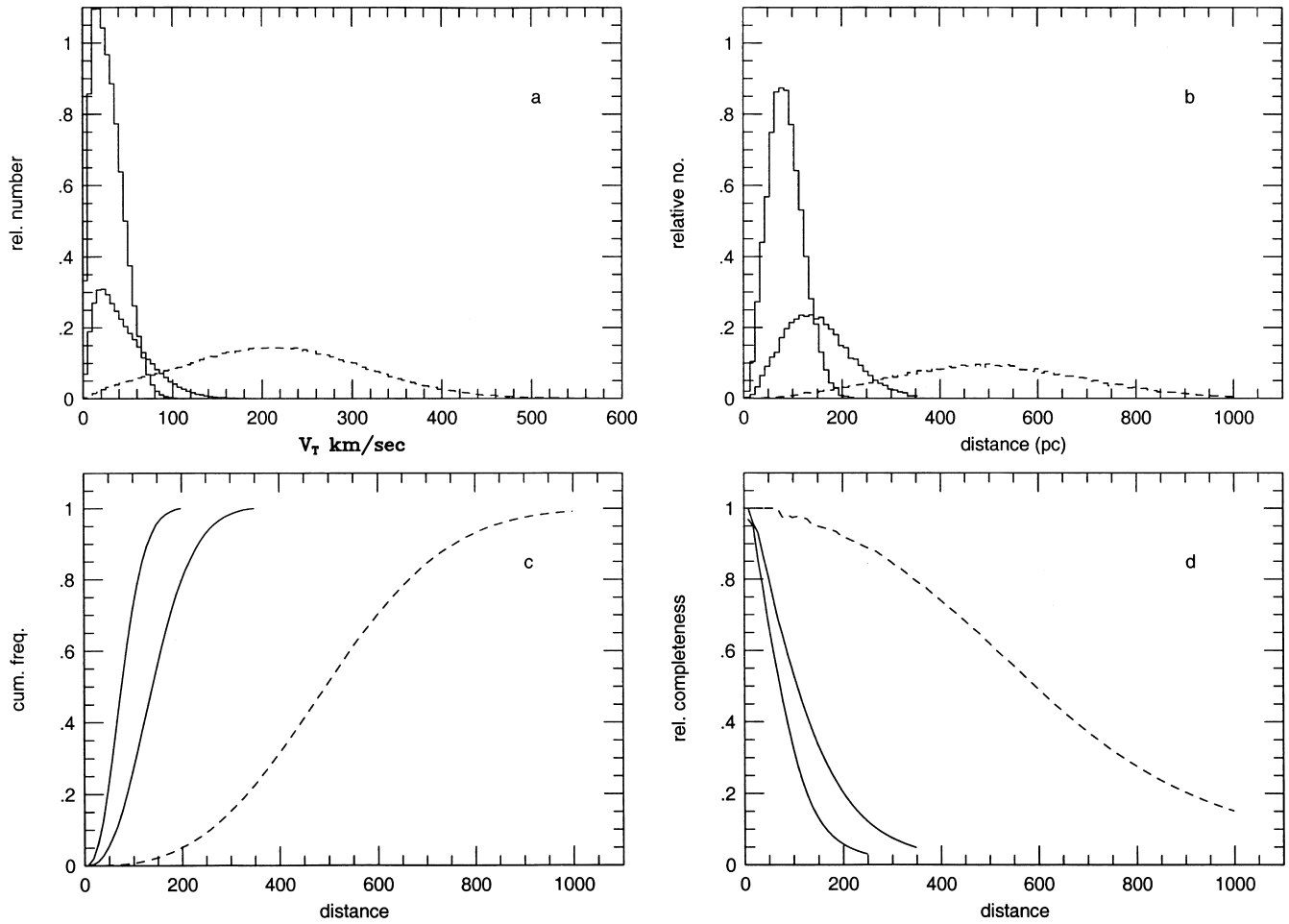

Figure 5. Simulations of the disc and halo velocity distributions toward SA94. (a) Predicted tangential velocity distributions for the disc and halo; (b) the predicted distance distribution of the two disc components (solid lines) and halo (dotted line) stars with $\mu > 0.1$ arcsec yr^{-1}; (c) predicted cumulative distributions of the proper-motion sample as a function of distance; (d) the fraction of disc and halo stars with $\mu > 0.1$ arcsec yr^{-1} in cumulative terms as a function of distance.

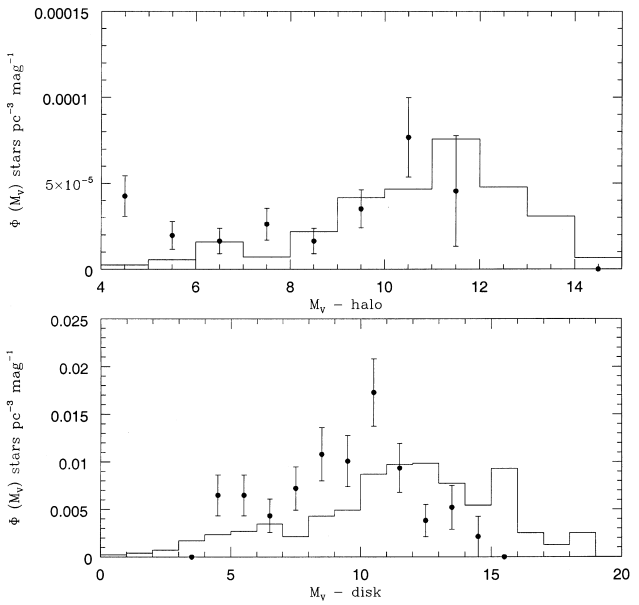

Figure 6. The luminosity functions for the disc and halo inferred from the SA94 proper-motion data. The reference luminosity functions are from Reid & Hawley (2000).

Table 6. Distance limits and selection functions

M_V	$N_{\rm disc}$	$N_{\rm halo}$	Disc(1)		Disc(2)		Halo	
			$d_{\rm C}$	f_μ	$d_{\rm C}$	f_μ	$d_{\rm C}$	f_μ
4.5	9	13	110	0.27	197	0.21	670	0.40
5.5	9	6	110	0.27	197	0.21	670	0.40
6.5	6	5	110	0.27	197	0.21	670	0.40
7.5	10	8	110	0.27	197	0.21	670	0.40
8.5	15	5	110	0.27	197	0.21	670	0.40
9.5	14	9	110	0.27	197	0.21	620	0.47
10.5	24	10	110	0.27	197	0.21	430	0.71
11.5	13	2	110	0.27	197	0.21	270	0.88
12.5	5	9	110	0.27	168	0.28	168	0.94
13.5	5	2	98	0.33	108	0.49	108	0.98
14.5	1	0	68	0.53	68	0.62	68	1.00

Unit at the Royal Observatory, Edinburgh, for providing photographic plate material for this project from the UK Schmidt Telescope (which is now operated by the Anglo-Australian Observatory) and for providing the measurements of the plates made using the SuperCOSMOS machine. We acknowledge helpful comments from the referee, and thank Clive Davenhall for assisting with access to Tycho-2 catalogue data.

REFERENCES

Cooke J. A., 1997, http://www.roe.ac.uk/cosmos/scospairing.html
Daou D. et al., 1994, The Digitized Sky Survey. Space Telescope Science Institute, Baltimore
Eichhorn H., Russell J., 1976, MNRAS, 174, 679
Evans D. W., 1992, MNRAS, 255, 521
Evans D. W., Irwin M., 1995, MNRAS, 277, 820
Gizis J. E., 1997, AJ, 113, 806
Gizis J. E., Reid I. N., 1998, AJ, 117, 508
Hanson R. B., 1979, MNRAS, 186, 875
Hawley S. L., Gizis J. E., Reid I. N., 1996, AJ, 112, 2799
Høg E. et al., 2000, The Tycho-2 Catalogue on CD-ROM, including Guide to Tycho-2. Copenhagen University Observatory, Copenhagen
Knox R. A., Hawkins M. R. S., Hambly N. C., 1999, MNRAS, 306, 736
Layden A. C., Hanson R. B., Hawlety S. L., Klemola A. R., Hanley C. J., 1996, AJ, 112, 2110
Lutz T. E., Upgren A. R., 1980, AJ, 85, 1390
Luyten W. J., 1979, LHS Catalogue. University of Minnesota, Minneapolis
Luyten W. J., 1979–1980, NLTT Catalogue. University of Minnesota, Minneapolis
Mould J. R., Wyckoff S., 1978, MNRAS, 182, 63
Murray C. A., 1986, MNRAS, 223, 649
Murray C. A., Corben P. M., 1979, MNRAS, 187, 723
Murray C. A., Argyle R. W., Corben P. M., 1986, MNRAS, 223, 629
Perryman M. A. C. et al., 1997, The Hipparcos and Tycho Catalogues. ESA, c/o ESTEC, Noordwijk
Reid I. N., 1984, MNRAS, 206, 1
Reid I. N., 1997, in Humphreys R. M., eds, ASP Conf. Ser. Vol. 127, Proper Motions and Galactic Astronomy. Astron. Soc. Pac., San Francisco, p. 63
Reid I. N., 1998, in Gilmore G., Howells D., eds, ASP Conf. Ser. Vol. 142, The 38th Herstmonceux Conference. Astron. Soc. Pac., San Francisco, p. 121
Reid I. N., Gizis J. E., 1997, AJ, 113, 2286
Reid I. N., Hawley S. L., 2000, New Light on Dark Stars. Springer-Verlag, Praxis
Reid I. N., Murray C. A., 1992, AJ, 103, 514
Reid I. N., Hawley S. L., Gizis J. E., 1995, AJ, 110, 1838
Röser S., Bastian U., 1991, PPM Star Catalogue. Astronomisches Rechen-Institut, Heidelberg
Schmidt M., 1975, ApJ, 202, 22
Urban S. E., Corbin T. E., Wycoff G. L., 1997, The ACT Reference Catalog. United States Naval Observatory, Washington DC

This paper has been typeset from a TEX/LATEX file prepared by the author.